Phase-resolved terahertz nanoimaging of math xmlns="http://www.w3.org/1998/Math/MathML">mrow>mi mathvariant="normal">W/mi>msub>mi>Te/mi>mn>2/mn>/msub>/mrow>/math> microcrystals

Ran Jing, Rocco A. Vitalone, Suheng Xu, Chiu Fan Bowen Lo, Zaiyao Fei, Elliott Runburg, Yinming Shao, Xinzhong Chen, Fabian Mooshammer, Alexander S. Mcleod, Mengkun Liu, Michael M. Fogler, David H. Cobden, Xiaodong Xu, and D. N. Basov

Phys. Rev. B **107**, 155413 — Published 10 April 2023

DOI: 10.1103/PhysRevB.107.155413

Phase-resolved terahertz nano-imaging of WTe_2 microcrystals

Ran Jing[1], Rocco A. Vitalone[1], Suheng Xu[1], Chiu Fan Bowen Lo[1], Zaiyao Fei[2], Elliott Runburg[2], Yinming Shao[1], Xinzhong Chen[3], Fabian Mooshammer[1], Alexander S. Mcleod[1], Mengkun Liu[3,4], Michael M. Fogler[5], David H. Cobden[2], Xiaodong Xu[2,6] and D. N. Basov[1]

[1]Department of Physics, Columbia University, New York, NY, USA

[2]Department of Physics, University of Washington, Seattle, WA, USA

[3]Department of Physics and Astronomy, Stony Brook University, Stony Brook, NY, USA

[4]National Synchrotron Light Source II, Brookhaven National Laboratory, Upton, NY, USA

[5]Department of Physics, University of California, San Diego, San Diego, CA, USA

[6]Department of Materials Science and Engineering, University of Washington, Seattle, WA, USA

Abstract:

The terahertz electrodynamics of few-layer WTe_2 is dominated by the plasmon response. However, terahertz surface plasmons with long wavelengths in two-dimensional exfoliated crystals are typically confined by the lateral geometry. Direct visualization of the plasmonic standing wave patterns is challenging due to the spatial confinement and low quality factor of the surface plasmon, especially for samples that are only a few monolayers thick. Here, we resolve subtle real-space features of the plasmonic response of WTe_2 by augmenting more common scattering amplitude experiments with the phase contrast accomplished within the time-domain version of THz nano-imaging. Amplitude and phase images allow us to quantitatively evaluate the evolution of the plasmonic response at cryogenic temperatures in samples with variable thickness from 3 to 12 monolayers. The proposed imaging modality is universally applicable to the THz near-field nanoscopy of low-dimensional materials.

Main Text:

Introduction

Scattering-type near-field microscopy (s-SNOM) is a powerful technique for exploring the nanoscale electrodynamics beyond the diffraction limit [1]. A conducting tip is used to enhance the electric field at the apex and scatters the incident light to the far field, resulting in a spatial resolution that depends only on the size of the tip apex (typically 30-200 nm) instead of the wavelength (typically 1-500 um) [2, 3]. The technique provides a wealth of data in experiments probing nano- and mesoscale phenomena, including polaritonic effects in low-dimensional systems [4, 5, 6, 7, 8, 9, 10], phase transitions in strongly correlated materials [11, 12, 13, 14, 15], the electrodynamics of photonic crystals [9, 16, 17] and free carrier distribution in nano-structured devices [18, 19].

At infrared and visible frequencies, the s-SNOM technique employs two major kinds of detection strategies: pseudo-heterodyne detection for continuous-wave (CW) illumination and Fourier-transformed infrared spectroscopy for broadband pulses. Both strategies modulate the tip-scattered signal by oscillating the tip vertically with respect to the sample surface. The near-field (NF) signal is subsequently demodulated at the integer harmonics of the tip oscillation frequency. For an imaging experiment with monochromatic lasers, pseudo-heterodyne interferometry is utilized to acquire both the amplitude and the phase of the artifact-free demodulated signal [20, 21, 22]. For spectroscopic studies using coherent broadband illumination, a Michelson interferometer is included in the light path to generate an interferogram, which is subsequently Fourier-transformed to determine the frequency-dependent NF contrast [23, 24]. Combining Fourier-transform infrared spectroscopy with real-space scanning produces hyper-spectral images that provide both spectrally and spatially dependent information. At Terahertz (THz) frequencies, the recent integration of quantum cascade lasers (QCL) [25, 26], THz transceivers [27], gas lasers [28, 29], and backward-wave oscillators [30] provide possible options for CW imaging. However, the available frequencies are still much more limited compared to QCLs in the mid-IR.

For nanoscale implementation of time-domain spectroscopy (TDS), high repetition rate broadband pulses generated with photoconductive antennas (PCAs) are widely utilized [15, 10, 19, 31, 32, 33, 34]. Recently, high-power broadband THz pulses generated using nonlinear optics, such as optical rectification [35] and tilted-pulse-front schemes, have also been applied in THz NF microscopy [36]. The THz signal is detected via two major approaches: white-light (WL) imaging and TDS. The white-light imaging resolves the E field at the main peak $\hat{E}$ of the time-domain THz pulse, corresponding to a spectrally integrated NF contrast [15, 19, 10, 32, 31, 33]. Since the materials have a complex optical response, $\hat{E}$ is associated with both the amplitude and the phase of the scattered radiation. While WL imaging provides integrated nanoscale THz contrast, it is impossible to recover the full complex NF signal including both amplitude and phase contrast using this approach. The TDS method [15, 31, 32, 37, 38, 39] yields the THz near-field amplitude and phase spectra via the Fourier transformation of the time-domain signal. However, TDS is not suitable for fast imaging, especially since hyper-spectroscopy (a combination of WL imaging and TDS) demands an exceedingly long data acquisition time. To circumvent these technical issues, we introduce here a novel phase-resolved detection method for pulsed illumination to rapidly access both the averaged amplitude and the phase information in broadband THz nano-imaging (nano-THz).

As a testbed for our new approach, we investigate mono- and few-layer tungsten ditelluride (WTe_2) microcrystals, which have attracted much attention due to the rich physical phenomena observed in this van der Waals layered material. For example, when patterned into narrow ribbons, WTe_2 microcrystals show hydrodynamic current flow below 20 K [40]. When thinned down, the transport properties of WTe_2 reveal a crossover from 3D to a 2D electronic system. Spin-orbit coupling (SOC) gradually drives the conduction and valence band away from the Fermi energy, leading to reduced sizes of electron and hole pockets in momentum space [41]. Few-layer WTe_2 further shows various quantum transport and photo-transport behaviors [42, 43, 44, 45] due to the low symmetry of the material. Additionally, an anisotropic plasma frequency [46, 47, 48] gives rise to in-plane hyperbolic plasmonic behavior [49]. To investigate the layer dependence of the Drude behavior on a micron-sized layered WTe_2 structure, we took the advantage of the nano-THz technology [36] to break through the diffraction limit and access the low energy electron response. In this letter, we report the phase-resolved imaging data collected by the new technique. The phase channel not only provides critical information to extract the electrodynamic property of the material, but also exhibits prominent real-space feature of propagating surface plasmon modes.

Detection of the carrier-envelope phase of terahertz pulses

In a previous study [36], we overcame the diffraction limit and used the traditional WL imaging technique to study the nanoscale THz response of WTe_2. We concluded that the temperature-dependent NF signal of 2L-12L WTe_2 is dominated by the surface plasmon (SP). In this report, we apply the phase-resolved NF imaging technique to acquire more detailed maps of the amplitude and phase of the scattered light. Experimental access to the full complex-valued NF signal has uncovered characteristic features of the plasmonic response of WTe_2 that remained obscured in our preliminary report. New data confirm that the WTe_2 plasmon has longer wavelength λ_P and higher quality factor Q at low temperature. We also found an increase in plasma frequency and a decrease in scattering rate at low temperatures. The complex-valued NF signals also facilitate the extraction of the complex permittivity of WTe_2 by modeling of the real-space patterns.

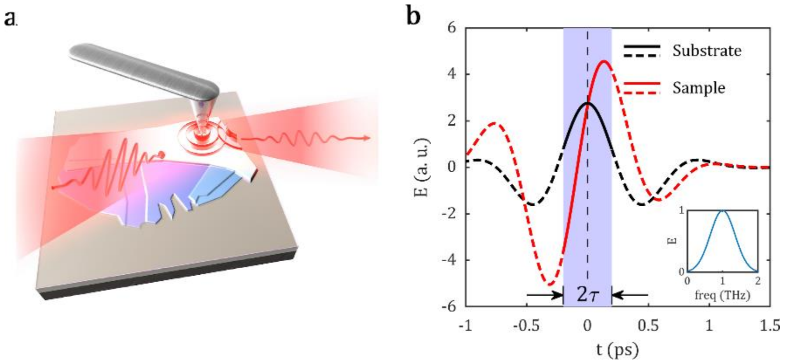

Figure 1|Sideband detection of THz near-field signal via time-delay modulation. **a** Schematic diagram of the experimental configuration in analogy to Ref. *[36]*. **b** Schematic time-domain THz signals of an insulating substrate and a conductive sample on the substrate. The signals are different in both amplitude and carrier-envelope phase (CEP). Due to the CEP shift, the main peaks of the sample and the substrate occur at different time points. The shaded area indicates the range of the modulation of the measurement time delay*.* The inset depicts the amplitude spectrum of the THz pulses.

The schematics of the proposed phase-resolved nano-THz experiments are displayed in Fig. 1. In these experiments, THz radiation is generated through optical rectification of optical pulses at 1030 nm (17 W at 750 kHz repetition rate) with a tilted phase front onto a $LiNbO_3$ single crystal. The generated THz beam is filtered to be a Gaussian beam with a center frequency of 1 THz and a full width at the half maximum of 200-300 GHz. The detection is achieved through EO sampling of the tip-scattered THz pulse in ZnTe crystal gated by 20-fs pulses at 800 nm. The THz beam is focused onto an 80-µm long PtIr wire tip from Rocky Mountain Nanotechnology. The tip oscillates and modulates the scattered NF signal at $\Omega \sim 70$ kHz. The detected signal is demodulated at the integer multiples of the tip oscillation frequency. Instead of detection at a fixed time delay (as in conventional WL imaging), we periodically modulate the time delay of the gate pulses at a frequency $M \ll \Omega$. Consequently, the detected amplitudes occur at carrier-band frequencies ($n\Omega$) and sideband frequencies ($n\Omega \pm mM$). Here, the carrier bands encode the in-phase part of the signal, and the first sidebands encode the out-of-phase part. By combining signals from different channels, the method provides a reliable estimation of the CEP. In the Supplemental Material [50],we provide a detailed description of the method.

Terahertz near-field signal of representative materials

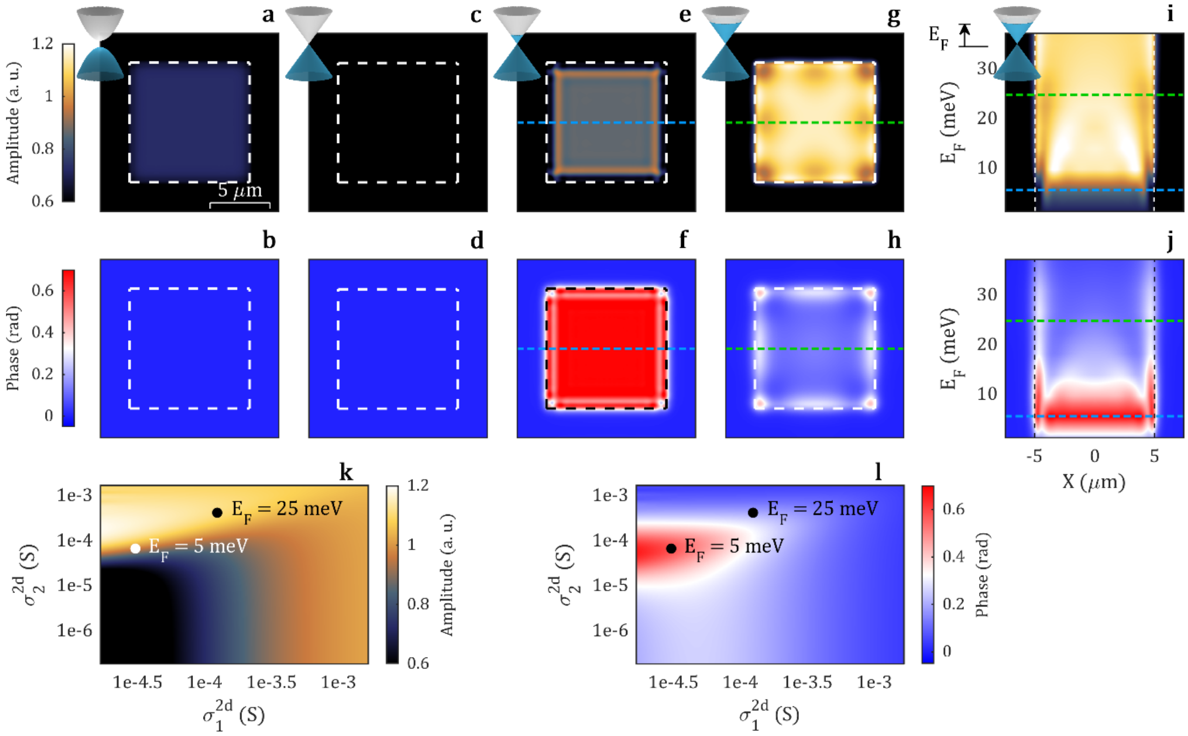

Figure 2| THz near-field amplitude and phase for representative materials. The simulated NF amplitude and phase of a 0.3-nm thin crystal. Panels **a** and **b** correspond to a band insulator, **c** and **d** to Dirac material with $\mu = 0$, **e** and **f** to Dirac material with $\mu = 5\ meV$, **g** and **h** to Dirac material with $\mu = 25\ meV$. The optical constants (conductivities) utilized for simulations are listed in Table 1. The simulations are calculated at $f = 1\ THz$ and T = 0 K. **i**, **j** Horizontal linecuts ($Y = 0$) of amplitude and phase are extracted for a range of chemical potentials ($\mu = 0 \sim 37.5\ meV$). **k**, **l** NF signal map of an infinitely large metallic sheet sample with arbitrary 2-dimensional conductivity $\sigma^{2d} = \sigma \cdot d$ at 1 THz. The dots mark the results of Dirac materials simulated at different chemical potentials.

To demonstrate the sensitivity of the THz NF amplitude and phase images to a material's optical constant (permittivity), we simulated signals at a representative frequency of 1 THz of a gapped insulator and Dirac semimetal at different doping levels

(Fig. 2). The parameters of the simulations are summarized in Table 1. The sample is assumed to be a 0.3-nm thick 10 μm × 10 μm square stacked on top of a SiO_2/Si substrate. The simulation is based on the real-space NF modeling documented in Ref. [36]. Since the simulation assumes T = 0 K, the impact of thermal doping is not considered. In this simulation, we assume the Dirac semimetal has a relatively low scattering rate $\gamma = 10\ \mathrm{cm}^{-1}$ to highlight the doping dependence of the NF signal. In the Supplemental Material [50], we also calculated results with a higher scattering rate, as reported, for example, in graphene [51]. For the gapped insulator with $\epsilon = 80$ (Fig. 2a and 2b), the difference in amplitude between the sample and the substrate is induced by the difference in ϵ_1 ($\epsilon_2 \sim 0$). The phase of the gapped insulator is identical to that of the substrate due to the lack of absorption. The neutral Dirac (Fig. 2c and 2d) material shows a negligible contrast with respect to the substrate. Because of the absence of free charges, only the interband transition contributes to the optical response. However, the quantum conductance is not strong enough to generate observable near-field contrast in either amplitude or phase channels.

	Band Insulator	Dirac Semimetal		
		$\mu = 0$	$\mu = 5$ meV	$\mu = 25$ meV
ϵ	80	$1 + 3700i$	$-4200 + 1900i$	$-2500 + 8000i$
σ_1^{2d}(S)	0	1×10^{-3}	5×10^{-4}	2.2×10^{-3}
$\lambda_P\ (\lambda_P^*), Q$	−	−	4 (1.9) μm, 2	24 (12) μm, 3

Table 1|The permittivity and conductivity of the simulated materials, the unscreened (screened) plasma wavelength λ_P (λ_P^*) and the Q-factor of the screened SPs in Fig. 1. The permittivity is calculated based on graphene band structure at $T = 0\ K$ and $\gamma = 10\ cm^{-1}$.

For doped Dirac materials (Fig. 2c-2h), the surface electrodynamics is dominated by the SPs. At low chemical potentials, the plasma frequency is low and comparable to the probing THz radiation. The weak oscillator strength gives rise to a low amplitude signal (Fig. 2e). However, because the probing frequency is close to the SP resonance, a strong phase response is observed (Fig. 2f). At higher chemical potentials, the plasma frequency increases. The real part of the dielectric function at 1THz becomes more negative, and the wavelength of the SP and the NF amplitude at 1 THz are increased (Fig. 2g). The up-shift of the plasma resonance frequency reduces the overall phase response at simulation frequency 1 THz (Fig. 2h). Because of the long wavelength of the SP screened by the substrate and the low quality factor, the clarity of the SP fringe pattern is suppressed. To study the chemical potential dependence (Fig. 2i and 2j), we extracted horizontal linecuts along the sample. With increasing chemical potentials, the plasma fringes with growing wavelength on opposite edges gradually merge and weaken in both channels. As a result, the most significant feature of SPs at high chemical potential is the local enhancement of phase images near the sample edge. Considering the entire doping dependence (vertical axes of Fig. 2j), the spatial modulation in scattering response is more apparent in the phase than in the amplitude channel. In Fig. 2k and 2l, we map out the near-field amplitude and phase for infinitely large sheet samples with arbitrary 2-dimensional conductivities $\sigma_{2d} = \sigma \cdot d$. By introducing the phase channel, we can estimate the conductivity or permittivity of the investigated sample based on Fig. 2k and 2l.

Results

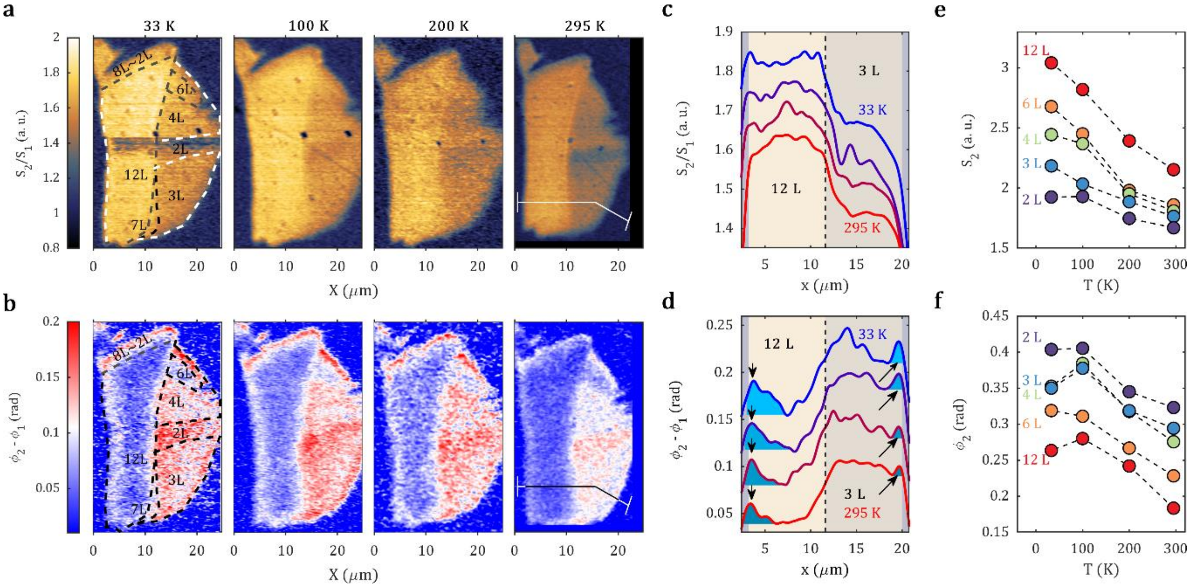

Figure 3| The phase-resolved THz imaging of a multi-terraced WTe2 microcrystal. **a**, **b** Temperature-dependent normalized amplitude (S_2/S_1) and phase images ($\phi_2 - \phi_1$) of WTe2 as a function of temperature. The data in each image are subsequently normalized on the SiO2/Si substrate. The boundaries of all terraces are demarcated with dashed lines in the images recorded at 33 K. Solid lines in the images taken at 295 K reveal the trajectory of the linecuts analyzed in panels c and d. **c** The amplitude and **d** phase linecuts extracted from **a** and **b**. The linecuts in both channels are shifted along the vertical axis for clarity. The modulations near the sample edges (marked with black arrows and highlighted with blue shading) extend into the 12L region; the width of these peaks depends strongly on the temperature. **e, f** Temperature-dependent unnormalized amplitude (S_2) and phase (ϕ_2) averaged over all pixels in each terrace.

We now demonstrate the utility of the phase-resolved WL imaging, using multi-terraced semimetallic WTe2 microcrystals as a case study. The configuration of our homebuilt THz-SNOM and THz generation and detection are schematically displayed in the Supplemental Material [50]. In this experiment, we focus on the demodulation at the 2nd harmonic frequency of tip oscillation. The exfoliated microcrystals of WTe2 have a variety of terraces. The boundaries of all regions are demarcated, and the layer numbers are labeled in Fig. 3a. The entire microcrystal is encapsulated between the top (6 nm) and bottom (20 nm) hexagonal boron nitride (hBN). The substrate of the structure is p-doped silicon with a 285-nm SiO2 cover layer.

The NF amplitude and phase of WTe2 are acquired from 33 K to 295 K (Fig. 3a and 3b). In near-field imaging, dividing the higher-order signal by the lower-order signal is proven to generate more generic near-field information [52]; thus the images and linecuts are presented as S_2/S_1 and $\phi_2 - \phi_1$. However, we observe that the ratio between signals of different orders depends strongly on the geometry of the near-field tip, which may change when scanning different images. As a result, tracking the temperature dependence of the signal level is difficult. Therefore, we use S_2 normalized on the subtrate in the same image to extract the averaged signal in Fig. 3e and 3f. With decreasing temperature (Fig. 3e), the amplitude recorded in 3L-12L regions increases, consistent with our earlier nano-THz experiment using conventional data acquisition [36]. The 2L region exhibits a slightly enhanced amplitude at low temperatures, in contrast to the previous study, where the signal on 2L is nearly temperature independent. The phase values for all regions are also higher at lower temperatures. As for the layer dependence, thicker WTe_2 regions show higher NF amplitude. The phase shows the opposite layer dependence.

The inconsistency between the 2L results here and the previous study [36] reveals the importance of acquiring the full complex-valued NF signal. Firstly, by incorporating the phase-resolved technique, we can separate the amplitude and phase degrees of freedom. Since 2L WTe_2 has a large phase compared to the substrate, the signal of 2L is delayed compared to that of the substrate. The WL time delay when scanning the 2L is not on the THz main peak. If we consider the main peak signal as the WL amplitude, the acquired signal on 2L will be significantly lower than the real WL amplitude due to the large phase contrast. Therefore, this phenomenon becomes more apparent at lower temperatures where the phase difference increases in magnitude.

As discussed in Ref. [36], the NF signal of few-layer WTe_2 is dominated by SP. In Fig. 3c and 3d, we extracted linecuts at identical locations in all images in Fig. 3a and 3b to demonstrate the real-space pattern of SP. At 295 K (Fig. 3c), the magnitude of the scattering amplitude in the middle of the 12 L WTe_2 region is higher than the that at the border. At the 33 K, the contrast between the center and the border of 12 L is absent. In the phase channel (Fig. 3d), peaks (indicated by arrows) are observed at all temperatures and on both 12L/substrate and 3L/substrate edges. To clearly illustrate the temperature dependence of the extent of the edge peak, phase linecuts in Fig. 3d are shifted vertically and the peaks are highlighted with blue shades. The peak becomes more prominent and extends more deeply into the sample at lower temperatures. As discussed below, the strong and systematic temperature and thickness dependence of the edge peak in the phase profile is an important indicator of the underlying optical properties of the microcrystals. In the Supplemental Material [50], we also provide spectroscopic results showing the consistency between the phase-resolved imaging and TDS.

Discussion

Simulations of nano-THz contrasts

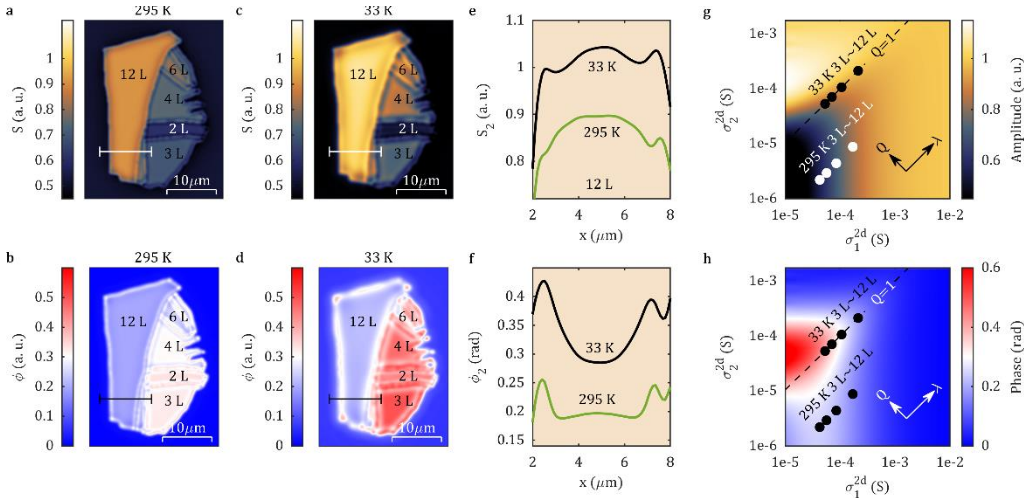

Figure 4| Real-space modeling of SP patterns in WTe2. **a** The amplitude and **b** phase images. Simulations adequately reproduce key features of the T = 295 K experimental data in Fig. 3 using permittivity values listed in Table 2. The values are based on Ref. [36]. **c**, **d** The simulated amplitude and phase are calculated at T = 33 K. **e**, **f** The simulated amplitude and phase linecuts of 12L WTe_2 at the location indicated in **a-d**, identical to those extracted from experiments. **g**, **h** We mark the estimated conductivities of 3L-12L WTe_2 on the near-field amplitude and phase map generated by the lightning-rod model [53]. The dashed line highlights conductivities corresponding to $Q = 1$.

To understand the imaging results, we simulated the real-space SP patterns at 295 K (Fig. 4a and 4b) and 33 K (Fig. 4c and 4d). The simulation assumes the NF signal of a 2D material is proportional to the z-direction (along the tip) polarization of a dipole at a certain height near the sample surface. The concept of this method has been successfully applied to model previous NF patterns at both THz [36] and mid-IR [54] [55] [56] frequencies. The permittivity (conductivity) values of all regions in Fig. 4a-4d are summarized in Table 2. The permittivity values used in the simulation are based on the model in Ref. [36] and the conclusions drawn in [36] that the 2 L - 12 L WTe_2 can be described by a semimetal with $\Delta = 10 - 20$ meV. The real-space simulation focuses on the SP pattern and the averaged signal is less important than that produced by the lightning-rod model presented in Fig. 4g and 4h. Nevertheless, the simulated signal shows the same layer number and temperature dependence as in the experiment.

Layer number	ϵ	$\sigma_{1,2d}$ (μS)	$\lambda_P, \lambda_P^*, Q$ of 2L or 12L
2L (295 K)	$-17(3) + i350(100)$	30	80 nm, 28 nm, 0.05
2L (33 K)	$-450(100) + i450(100)$	36	2 μm, 0.69μm, 1
3L-12L (295 K)	$-30(5) + i600(200)$	$20 \times N$	$67 \times$ N nm, $23 \times$ N nm, 0.05 0.8 μm, 0.3 μm for 12L
3L-12L (33 K)	$-760(200) + i760(200)$	$30 \times N$	$1.7 \times N$ μm, $0.58 \times$ N μm, 1 20 μm, 7 μm for 12L

Table 2|The permittivity of each region in the simulation in Fig. 4a and 4b. The permittivity value is estimated based on Ref. *[36]*. We also estimated the uncertainty of the simulated permittivity based on the quality of the simulation. For 3L-12L, the wavelength is proportional to the layer number N. We note that the difference in the NF signal of 3L-12L is solely caused by the difference in sample thickness.

We extracted linecuts (Fig. 4e and 4f) in the simulation to compare with the experiment result on 12 L. In both the 33K and the 295 K simulation result, we observe the same narrow edge peak in the phase channel as in the experiment. From 295 K to 33 K, the wavelength of the simulated SP increased by an order of magnitude even though we do not observe a change in the length scale of the real-space pattern proportional to the wavelength. The reasons are the low quality factor of the plasmon and the small size of the sample. The amplitude is boosted and flattened, which agrees with the experiment as well.

Besides the real-space pattern, we mark the conductivities (permittivities) for 3L-12L WTe2 in the NF signal map in Fig. 4g and 4h together with the increase in wavelength and quality factor. Because we assume 3L-12L WTe2 shares the same optical constant, the 2d conductivities of different regions are along a diagonal line corresponding to a specific quality factor at each temperature. The maps clearly show that the dominating factor in the increase in amplitude and phase on WTe2 from 295 K to 33 K is the dramatic increase in the quality factor. The fast lengthening of the wavelength at 33 K boosts the value of $\sigma_{1,2d}$, consistent with the transport measurement [57].

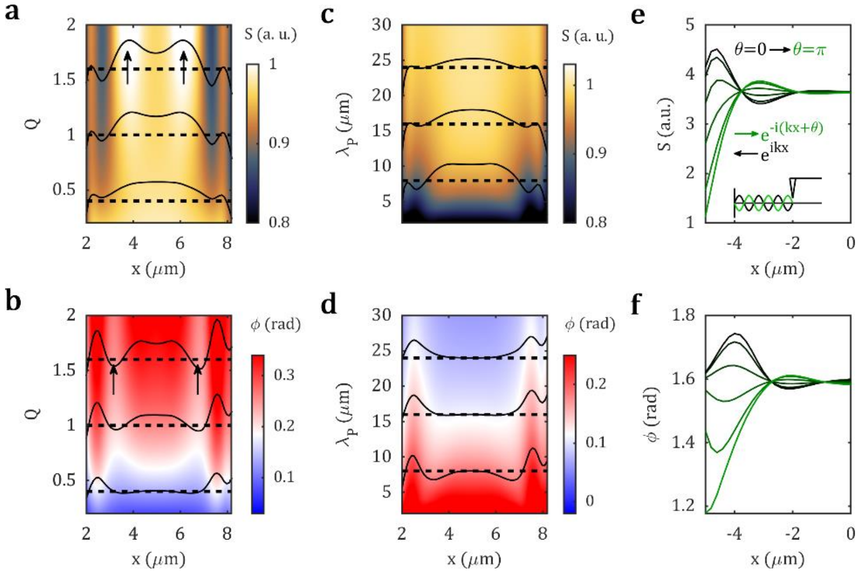

Fig 5| Simulating THz plasma fringe patterns. In **a** and **b**, we maintain the wavelength $\lambda_P = 10\ \mu m$ and tune the Q-factor. The Q-factor dependence of the amplitude and phase linecuts are shown in false-color images. We highlight three curves with $Q = 0.4$, 1, and 1.6. The plasmon fringe is indicated by black arrows. In **c** and **d**, we maintain the Q-factor $Q = 0.5$ and tune the wavelength λ_P. We highlight three curves with $\lambda_P = 8$, 16, and 24 μm. **e**, **f** The SP pattern depends critically on the phase shift θ in the process of SP reflection from the sample edge. The θ dependence of the SP pattern is plotted. In the inset, we illustrate the phase shift acquired by the reflected SP wave.

To exhibit the λ_P and Q dependence of the SP pattern, we tuned both parameters in a wide range in the simulation. By increasing the Q-factor from 0.2 to 2 (Fig. 5a and 5b) and maintaining $\lambda_P = 10$ μm, the amplitude fringe (indicated by black arrows in Fig. 5a) becomes visible. In the phase channel (Fig. 5b), the overall value increases with increasing Q-factor and the phase fringe (indicated by black arrows) becomes visible as well. In Fig. 5c and 5d, we demonstrate the λ_P dependence of the SP pattern by fixing the Q-factor at 0.5. The wavelength dependence of the overall value is analogous to the result shown in Fig. 2i and 2j. The longer λ_P diminishes the visibility of the plasmon fringe in both the amplitude and phase channels due to the limited sample size.

The SP pattern is determined by the phase shift θ acquired by the reflected wave from the sample edge (inset of Fig. 5e). In Fig. 5e and 5f, we demonstrate modeling with

$\theta = 0 - \pi$. To emphasize the features near the edge, the model calculates an SP with screened wavelength $\lambda_P^* = 8$ μm and $Q = 0.25$ at 1 THz near the left end of a one-dimensional ribbon ($L = 10$ μm). Because of the screening of the p-doped Si, the dispersion of the SP is close to linear, and therefore the wave packet is not distorted in the propagation. In the amplitude channel (Fig. 5e), the signal on the edge gradually decreases with increasing θ. When $\theta = \pi$, the wave reflection is analogous to mechanical waves propagating on a string with a fixed end, leading to a low response near the edge. In the phase channel (Fig. 5f), the peak near the edge becomes a valley at a high phase shift. Compared to higher frequencies, THz-range SPs are more easily screened by the metallic gating material beneath the sample due to their long wavelengths. Therefore, the screened plasmon acquires a reflection phase shift $\theta = 0$ [58]. In the current sample configuration, the Si substrate is highly p-doped and shows moderate metallicity ($\rho = 0.01 - 0.02\,\Omega \cdot \mathrm{cm}$). Accordingly, the SP reflection phase shift is tuned to 0 in the modeling in Fig. 4 and Fig. 5a-5d, which matches reasonably well with the experimental data.

Because the illumination in the experiment is pulsed instead of CW, we must consider the launching and detection of the SP pattern in the time domain. As shown in the inset of Fig. 5e, the signal is the interference between the tip-launched plasmon and the edge-reflected plasmon. The edge-reflected plasmon is launched by the tip at an earlier time point. For WTe_2, the speed of the propagating SP is estimated to be on the order of $v \sim 10$ μm/ps [36]. Therefore, the reflected wave takes a non-negligible time (~picoseconds) to travel back to the tip. In this experiment, we detect near the main peak $\hat{E}$ of the pulse. The reflected wave is launched at an earlier time t when the THz excitation field is lower. This phenomenon induces an artificial damping factor to the observed SP fringe. We therefore predict that SP fringe patterns can be more easily observed at a larger time delay than the main peak. More details are documented in the Supplemental Material [50].

In conclusion, we devised, implemented, and validated a sideband detection method capable of extracting the averaged amplitude and phase of broadband THz signals. We demonstrate the utility of the novel imaging modalities for few-layer WTe_2. With a small time-delay oscillation, the in-phase and out-of-phase frequency components of the signal encoded in alternating carrier-bands and sidebands can be easily detected through lock-in amplification. Applying this method to the nano-THz investigation of a multi-terraced semimetallic WTe_2 microcrystal, we demonstrated the NF amplitude and phase pattern of an SP confined in a relatively small sample geometry. We simulated the SP pattern over a broad parameter space of plasmonic wavelength, quality factor, sample thickness, etc. By comparing these simulations with the experiment, we extracted the permittivity of few-layer WTe_2. The advantage of the sideband detection method over traditional white-light imaging is that the amplitude and the phase degrees of freedom can be independently extracted. The full complex-valued signal provided by the method is the key to studying the damped plasmonic and polaritonic behaviors at THz frequencies and applies to metallic as well as dielectric systems. Compared to hyper-spectral imaging, this represents a practical method to efficiently achieve averaged phase information in the challenging THz frequency range with less beam time and fewer resource requirements.

Acknowledgements

Research at Columbia on electrodynamics of WTe_2 is solely supported as part of Programmable Quantum Materials, an Energy Frontier Research Center funded by the U.S. Department of Energy (DOE), Office of Science, Basic Energy Sciences (BES), under award DE-SC0019443. Development of nano-THz instrumentation is supported by the Vannevar Bush Faculty Fellow program ONR-VB: N00014-19-1-2630.

Bibliography

[1] L. Novotny, "The history of near-field optics," *Progress in optics,* vol. 50, p. 137, 2007.

[2] Y. Inouye and S. Kawata, "Near-field scanning optical microscope with a metallic probe tip," *Optics letters,* vol. 19, p. 159–161, 1994.

[3] B. Knoll and F. Keilmann, "Enhanced dielectric contrast in scattering-type scanning near-field optical microscopy," *Optics communications,* vol. 182, p. 321–328, 2000.

[4] Z. Fei, A. S. Rodin, G. O. Andreev, W. Bao, A. S. McLeod, M. Wagner, L. M. Zhang, Z. Zhao, M. Thiemens, G. Dominguez and others, "Gate-tuning of graphene plasmons revealed by infrared nano-imaging," *Nature,* vol. 487, p. 82–85, 2012.

[5] J. Chen, M. Badioli, P. Alonso-González, S. Thongrattanasiri, F. Huth, J. Osmond, M. Spasenović, A. Centeno, A. Pesquera, P. Godignon and others, "Optical nano-imaging of gate-tunable graphene plasmons," *Nature,* vol. 487, p. 77–81, 2012.

[6] S. Dai, Q. Ma, M. K. Liu, T. Andersen, Z. Fei, M. D. Goldflam, M. Wagner, K. Watanabe, T. Taniguchi, M. Thiemens and others, "Graphene on hexagonal boron nitride as a tunable hyperbolic metamaterial," *Nature nanotechnology,* vol. 10, p. 682–686, 2015.

[7] G. Ni, d. A. S. McLeod, Z. Sun, L. Wang, L. Xiong, K. W. Post, S. S. Sunku, B.-Y. Jiang, J. Hone, C. R. Dean and others, "Fundamental limits to graphene plasmonics," *Nature,* vol. 557, p. 530–533, 2018.

[8] A. J. Sternbach, S. Latini, S. Chae, H. Hübener, U. De Giovannini, Y. Shao, L. Xiong, Z. Sun, N. Shi, P. Kissin and others, "Femtosecond exciton dynamics in WSe 2 optical waveguides," *Nature communications,* vol. 11, p. 1–6, 2020.

[9] S. S. Sunku, G. Ni, B.-Y. Jiang, H. Yoo, A. Sternbach, A. S. McLeod, T. Stauber, L. Xiong, T. Taniguchi, K. Watanabe and others, "Photonic crystals for nano-light in moiré graphene superlattices," *Science,* vol. 362, p. 1153–1156, 2018.

[10] J. Zhang, X. Chen, S. Mills, T. Ciavatti, Z. Yao, R. Mescall, H. Hu, V. Semenenko, Z. Fei, H. Li and others, "Terahertz nanoimaging of graphene," *ACS Photonics,* vol. 5, p. 2645–2651, 2018.

[11] M. M. Qazilbash, M. Brehm, B.-G. Chae, P.-C. Ho, G. O. Andreev, B.-J. Kim, S. J. Yun, A. V. Balatsky, M. B. Maple, F. Keilmann and others, "Mott transition in VO2 revealed by infrared spectroscopy and nano-imaging," *Science,* vol. 318, p. 1750–1753, 2007.

[12] M. K. Liu, M. Wagner, E. Abreu, S. Kittiwatanakul, A. McLeod, Z. Fei, M. Goldflam, S. Dai, M. M. Fogler, J. Lu and others, "Anisotropic electronic state via spontaneous phase separation in strained vanadium dioxide films," *Physical review letters,* vol. 111, p. 096602, 2013.

[13] M. Liu, A. J. Sternbach and D. N. Basov, "Nanoscale electrodynamics of strongly correlated quantum materials," *Reports on Progress in Physics,* vol. 80, p. 014501, 2016.

[14] A. S. McLeod, E. Van Heumen, J. G. Ramirez, S. Wang, T. Saerbeck, S. Guenon, M. Goldflam, L. Anderegg, P. Kelly, A. Mueller and others, "Nanotextured phase coexistence in the correlated insulator V 2 O 3," *Nature Physics,* vol. 13, p. 80–86, 2017.

[15] H. T. Stinson, A. Sternbach, O. Najera, R. Jing, A. S. Mcleod, T. V. Slusar, A. Mueller, L. Anderegg, H. T. Kim, M. Rozenberg and others, "Imaging the nanoscale phase separation in vanadium dioxide thin films at terahertz frequencies," *Nature communications,* vol. 9, p. 1–9, 2018.

[16] L. Xiong, C. Forsythe, M. Jung, A. S. McLeod, S. S. Sunku, Y. M. Shao, G. X. Ni, A. J. Sternbach, S. Liu, J. H. Edgar and others, "Photonic crystal for graphene plasmons," *Nature communications,* vol. 10, p. 1–6, 2019.

[17] F. J. Alfaro-Mozaz, S. G. Rodrigo, P. Alonso-González, S. Vélez, I. Dolado, F. Casanova, L. E. Hueso, L. Martín-Moreno, R. Hillenbrand and A. Y. Nikitin, "Deeply subwavelength phonon-polaritonic crystal made of a van der Waals material," *Nature communications,* vol. 10, p. 1–7, 2019.

[18] A. J. Huber, F. Keilmann, J. Wittborn, J. Aizpurua and R. Hillenbrand, "Terahertz near-field nanoscopy of mobile carriers in single semiconductor nanodevices," *Nano letters,* vol. 8, p. 3766–3770, 2008.

[19] Z. Yao, V. Semenenko, J. Zhang, S. Mills, X. Zhao, X. Chen, H. Hu, R. Mescall, T. Ciavatti, S. March and others, "Photo-induced terahertz near-field dynamics of graphene/InAs heterostructures," *Optics express,* vol. 27, p. 13611–13623, 2019.

[20] L. Gomez, R. Bachelot, A. Bouhelier, G. P. Wiederrecht, S.-h. Chang, S. K. Gray, F. Hua, S. Jeon, J. A. Rogers, M. E. Castro and others, "Apertureless scanning near-field optical microscopy: a comparison between homodyne and heterodyne approaches," *JOSA B,* vol. 23, p. 823–833, 2006.

[21] N. Ocelic, A. Huber and R. Hillenbrand, "Pseudoheterodyne detection for background-free near-field spectroscopy," *Applied Physics Letters,* vol. 89, p. 101124, 2006.

[22] A. J. Sternbach, J. Hinton, T. Slusar, A. S. McLeod, M. K. Liu, A. Frenzel, M. Wagner, R. Iraheta, F. Keilmann, A. Leitenstorfer and others, "Artifact free time resolved near-field spectroscopy," *Optics Express,* vol. 25, p. 28589–28611, 2017.

[23] S. Amarie, T. Ganz and F. Keilmann, "Mid-infrared near-field spectroscopy," *Optics Express,* vol. 17, p. 21794–21801, 2009.

[24] M. Brehm, A. Schliesser and F. Keilmann, "Spectroscopic near-field microscopy using frequency combs in the mid-infrared," *Optics express,* vol. 14, p. 11222–11233, 2006.

[25] M. C. Giordano, S. Mastel, C. Liewald, L. L. Columbo, M. Brambilla, L. Viti, A. Politano, K. Zhang, L. Li, A. G. Davies and others, "Phase-resolved terahertz self-detection near-field microscopy," *Optics express,* vol. 26, p. 18423–18435, 2018.

[26] E. A. A. Pogna, L. Viti, A. Politano, M. Brambilla, G. Scamarcio and M. S. Vitiello, "Mapping propagation of collective modes in Bi2Se3 and Bi2Te2. 2Se0. 8 topological insulators by near-field terahertz nanoscopy," *Nature communications,* vol. 12, p. 1–11, 2021.

[27] C. Liewald, S. Mastel, J. Hesler, A. J. Huber, R. Hillenbrand and F. Keilmann, "All-electronic terahertz nanoscopy," *Optica,* vol. 5, p. 159–163, 2018.

[28] P. Alonso-González, A. Y. Nikitin, Y. Gao, A. Woessner, M. B. Lundeberg, A. Principi, N. Forcellini, W. Yan, S. Vélez, A. J. Huber and others, "Acoustic terahertz graphene plasmons revealed by photocurrent nanoscopy," *Nature nanotechnology,* vol. 12, p. 31–35, 2017.

[29] S. Chen, A. Bylinkin, Z. Wang, M. Schnell, G. Chandan, P. Li, A. Y. Nikitin, S. Law and R. Hillenbrand, "Real-space nanoimaging of THz polaritons in the topological insulator Bi2Se3," *arXiv preprint arXiv:2107.10791,* 2021.

[30] Q. Lu, A. T. Bollinger, X. He, R. Sundling, I. Bozovic and A. Gozar, "Surface Josephson plasma waves in a high-temperature superconductor," *npj Quantum Materials,* vol. 5, p. 1–8, 2020.

[31] K. Moon, H. Park, J. Kim, Y. Do, S. Lee, G. Lee, H. Kang and H. Han, "Subsurface nanoimaging by broadband terahertz pulse near-field microscopy," *Nano letters,* vol. 15, p. 549–552, 2015.

[32] K. Moon, Y. Do, M. Lim, G. Lee, H. Kang, K.-S. Park and H. Han, "Quantitative coherent scattering spectra in apertureless terahertz pulse near-field microscopes," *Applied Physics Letters,* vol. 101, p. 011109, 2012.

[33] X. Chen, X. Liu, X. Guo, S. Chen, H. Hu, E. Nikulina, X. Ye, Z. Yao, H. A. Bechtel, M. C. Martin and others, "THz near-field imaging of extreme subwavelength metal structures," *ACS Photonics,* vol. 7, p. 687–694, 2020.

[34] A. Pizzuto, D. M. Mittleman and P. Klarskov, "Laser THz emission nanoscopy and THz nanoscopy," *Optics express,* vol. 28, p. 18778–18789, 2020.

[35] M. Plankl, P. E. Faria Junior, F. Mooshammer, T. Siday, M. Zizlsperger, F. Sandner, F. Schiegl, S. Maier, M. A. Huber, M. Gmitra and others, "Subcycle contact-free nanoscopy of ultrafast

interlayer transport in atomically thin heterostructures," *Nature Photonics,* vol. 15, p. 594–600, 2021.

[36] R. Jing, Y. Shao, Z. Fei, C. F. B. Lo, R. A. Vitalone, F. L. Ruta, J. Staunton, W. J.-C. Zheng, A. S. Mcleod, Z. Sun and others, "Terahertz response of monolayer and few-layer WTe2 at the nanoscale," *Nature communications,* vol. 12, p. 1–9, 2021.

[37] D. Grischkowsky, S. Keiding, M. Van Exter and C. Fattinger, "Far-infrared time-domain spectroscopy with terahertz beams of dielectrics and semiconductors," *JOSA B,* vol. 7, p. 2006–2015, 1990.

[38] R. Ulbricht, E. Hendry, J. Shan, T. F. Heinz and M. Bonn, "Carrier dynamics in semiconductors studied with time-resolved terahertz spectroscopy," *Reviews of Modern Physics,* vol. 83, p. 543, 2011.

[39] P. U. Jepsen, D. G. Cooke and M. Koch, "Terahertz spectroscopy and imaging–Modern techniques and applications," *Laser & Photonics Reviews,* vol. 5, p. 124–166, 2011.

[40] U. Vool, A. Hamo, G. Varnavides, Y. Wang, T. X. Zhou, N. Kumar, Y. Dovzhenko, Z. Qiu, C. A. C. Garcia, A. T. Pierce and others, "Imaging phonon-mediated hydrodynamic flow in WTe2," *Nature Physics,* p. 1–5, 2021.

[41] F.-X. Xiang, A. Srinivasan, Z. Z. Du, O. Klochan, S.-X. Dou, A. R. Hamilton and X.-L. Wang, "Thickness-dependent electronic structure in WTe 2 thin films," *Physical Review B,* vol. 98, p. 035115, 2018.

[42] Q. Ma, S.-Y. Xu, H. Shen, D. MacNeill, V. Fatemi, T.-R. Chang, A. M. M. Valdivia, S. Wu, Z. Du, C.-H. Hsu and others, "Observation of the nonlinear Hall effect under time-reversal-symmetric conditions," *Nature,* vol. 565, p. 337, 2019.

[43] K. Kang, T. Li, E. Sohn, J. Shan and K. F. Mak, "Nonlinear anomalous Hall effect in few-layer WTe 2," *Nature materials,* vol. 18, p. 324, 2019.

[44] Q. Wang, J. Zheng, Y. He, J. Cao, X. Liu, M. Wang, J. Ma, J. Lai, H. Lu, S. Jia and others, "Robust edge photocurrent response on layered type II Weyl semimetal WTe 2," *Nature Communications,* vol. 10, p. 1–7, 2019.

[45] S.-Y. Xu, Q. Ma, H. Shen, V. Fatemi, S. Wu, T.-R. Chang, G. Chang, A. M. M. Valdivia, C.-K. Chan, Q. D. Gibson and others, "Electrically switchable Berry curvature dipole in the monolayer topological insulator WTe 2," *Nature Physics,* vol. 14, p. 900, 2018.

[46] A. J. Frenzel, C. C. Homes, Q. D. Gibson, Y. M. Shao, K. W. Post, A. Charnukha, R. J. Cava and D. N. Basov, "Anisotropic electrodynamics of type-II Weyl semimetal candidate WTe 2," *Physical Review B,* vol. 95, p. 245140, 2017.

[47] C. C. Homes, M. N. Ali and R. J. Cava, "Optical properties of the perfectly compensated semimetal WTe 2," *Physical Review B,* vol. 92, p. 161109, 2015.

[48] Y. Shao, R. Jing, S. H. Chae, C. Wang, Z. Sun, E. Emmanouilidou, S. Xu, D. Halbertal, B. Li, A. Rajendran and others, "Nonlinear nanoelectrodynamics of a Weyl metal," *Proceedings of the National Academy of Sciences,* vol. 118, p. e2116366118, 2021.

[49] C. Wang, S. Huang, Q. Xing, Y. Xie, C. Song, F. Wang and H. Yan, "Van der Waals thin films of WTe 2 for natural hyperbolic plasmonic surfaces," *Nature communications,* vol. 11, p. 1–9, 2020.

[50] See Supplemental Material at [URL] for details about the phase-resolved method, additional simulation and extended data.

[51] P. Gallagher, C.-S. Yang, T. Lyu, F. Tian, R. Kou, H. Zhang, K. Watanabe, T. Taniguchi and F. Wang, "Quantum-critical conductivity of the Dirac fluid in graphene," *Science,* vol. 364, p. 158–162, 2019.

[52] L. Mester, A. A. Govyadinov and R. Hillenbrand, "High-fidelity nano-FTIR spectroscopy by on-pixel normalization of signal harmonics," *Nanophotonics,* vol. 11, p. 377–390, 2022.

[53] A. S. McLeod, P. Kelly, M. D. Goldflam, Z. Gainsforth, A. J. Westphal, G. Dominguez, M. H. Thiemens, M. M. Fogler and D. N. Basov, "Model for quantitative tip-enhanced spectroscopy and the extraction of nanoscale-resolved optical constants," *Physical Review B,* vol. 90, p. 085136, 2014.

[54] A. Y. Nikitin, P. Alonso-González, S. Vélez, S. Mastel, A. Centeno, A. Pesquera, A. Zurutuza, F. Casanova, L. E. Hueso, F. H. L. Koppens and others, "Real-space mapping of tailored sheet and edge plasmons in graphene nanoresonators," *Nature Photonics,* vol. 10, p. 239–243, 2016.

[55] D. J. Rizzo, B. S. Jessen, Z. Sun, F. L. Ruta, J. Zhang, J.-Q. Yan, L. Xian, A. S. McLeod, M. E. Berkowitz, K. Watanabe and others, "Charge-transfer plasmon polaritons at graphene/α-RuCl3 interfaces," *Nano letters,* vol. 20, p. 8438–8445, 2020.

[56] S. Xu, A. S. McLeod, X. Chen, D. J. Rizzo, B. S. Jessen, Z. Yao, Z. Wang, Z. Sun, S. Shabani, A. N. Pasupathy and others, "Deep Learning Analysis of Polaritonic Wave Images," *ACS nano,* vol. 15, p. 18182–18191, 2021.

[57] Z. Fei, T. Palomaki, S. Wu, W. Zhao, X. Cai, B. Sun, P. Nguyen, J. Finney, X. Xu and D. H. Cobden, "Edge conduction in monolayer WTe 2," *Nature Physics,* vol. 13, p. 677, 2017.

[58] B.-Y. Jiang, E. J. Mele and M. M. Fogler, "Theory of plasmon reflection by a 1D junction," *Optics express,* vol. 26, p. 17209–17226, 2018.